On-demand aerodynamics in integrally actuated membranes with feedback control

Stefano Buoso* and Rafael Palacios†

Imperial College, London, SW7 2AZ, United Kingdom

This paper is a numerical investigation on model reduction and control system design of integrally actuated membrane wings. A high-fidelity electro-aeromechanical model is used for the simulation of the dynamic fluid-structure interaction between a low-Reynolds-number flow and a dielectric elastomeric wing. Two reduced-order models with different levels of complexity are then derived. They are based on the projection of the full-order discretisation of fluid and structure on modal shapes obtained from eigenvalue analysis and Proper Orthogonal Decomposition. The low-order systems are then used for the design of Proportional-Integral-Derivative and Linear Quadratic Gaussian feedback schemes to control wing lift. When implemented in the full-order model, closed-loop dynamics are in very good agreement with the reduced-order model for both tracking and gust rejection, demonstrating the suitability of the approach. The control laws selected in this work were found to be effective only for low-frequency disturbances due to the large phase delay introduced by the fluid convective time-scales, but results demonstrate the potential for the aerodynamic control of membrane wings in outdoor flight using dielectric elastomers.

Nomenclature

a	Modal amplitude	E_i	Electric field vector
C_{ij}	Left Cauchy deformation tensor	F_{ij}	Deformation gradient
C_l	Lift coefficient	J	Determinant of the deformation gradient
C_p	Pressure coefficient	J_m	Gent model material constant

*Research associate, Department of Aeronautics.

†Reader, Department of Aeronautics, 355 Roderic Hill Building; r.palacios@imperial.ac.uk. AIAA Member.

K	Controller gain, penalty factor	ρ	Density
P	Pressure	σ_{ij}	Stress tensor component
q_i	System states	Φ_{ij}	Projection matrix
S_{ij}	snapshot matrix	φ	Base function
U	Volumetric strain energy function		
V	Velocity magnitude, voltage, volume	***Subscripts and Superscripts***	
v_i	Velocity vector	e	Electromechanical
W	Electromechanical strain energy function	m	Mechanical

Greek Letters		ν	Viscous
α	Angle of attack	s	Structural
ϵ	Dielectric permittivity	V	Voltage
λ	Stretch	∞	Equilibrium elastic, Free streem
μ	Shear modulus	0	Initial, Reference, Vacuum
ν	Poisson ratio		

I. Introduction

The development of advanced Micro Air Vehicles (MAVs) requires computational methods capable of characterising the dynamics of highly compliant structures in low-Reynolds-number flows. The main driver is the maximisation of efficiency to meet the stringent power and weight limitations of these vehicles. Experimental results at typical flying regimes of MAVs have shown that, thanks to their compliance, membrane wings exhibit delayed stall and higher maximum lift than their rigid counterparts [1, 2]. From a flight dynamics point of view, fixed-wings built with membranes have also shown higher manoeuvrability, agility and enhanced stability to small flow disturbances [3, 4]. Despite these advantages, low-speed controllability of fixed-wing MAVs remains one of the main issues that needs to be solved for outdoor flight. A promising strategy is the use of embedded actuation through the use of Dielectric Elastomers (DE) as the membrane material. This combines the advantages of membrane wings with a simple and lightweight control mechanism and could result in increased stability and controllability and lead towards "on-demand" aerodynamic performance. Recently, Hays et al. [5] and Curet et al. [6] have tested the use of DEs to increase

the performance of membrane wings through open-loop static and dynamic actuation. Low actuation authority was found at low angles of attack, with amplitudes of the oscillations being mostly independent on the voltage frequency. For larger angles the mean lift coefficient increased up to 20% but at the cost of large amplitude oscillations. A delayed in stall angle of up to $5^\circ - 7^\circ$ was also observed, which is consistent with previous experiments on non-actuated membranes [7]. However, issues of material stability and the high-voltage requirements would need to be addressed before actual deployment as MAV wing skins [8]. In particular, the required voltage for actuation depends on the membrane thickness and can reach several kilovolts for 1 mm thick wings.

Future design of such platforms will benefit from computational models that help describing the complex physical mechanisms in the interactions between the actuated membrane and the surrounding fluid. Several coupled models for passive membrane wings have been proposed in the literature [9, 10, 11]. Buoso and Palacios [12] have extended them to a fully coupled electro-aeromechanical wing model and investigated the open-loop response of the actuated membrane. The actuation has shown to provide enough authority to drive the dynamic response of the system, with peaks of lift coefficient up to twice the reference, non-actuated one. Those analysis are based on a membrane thickness of 50 μm, which requires voltage amplitudes of the order of 500 V. To date, however, there have been no previous experimental or numerical studies on the DE membrane performance in closed-loop.

Flow control in these flow regimes has mostly been investigated to suppress vortex-induced vibrations of bluff bodies. Open-loop and closed-loop control schemes based on Proportional-Integral-Derivative (PID) and state-feedback laws have been successfully demonstrated in this context [13, 14]. However, large time delays have also been observed for low-Reynolds-number flows. They demand very large integral gains and have shown to be quite challenging for control system design [7, 14]. Tregidgo et al. [7] showed the presence of a time-lag between the structural and fluid responses which was varying according to the flow conditions. Additionally, large delays in the response of actuated wings in low-Reynolds number flows have been measured by Williams et al. [15] who used feed-forward

control schemes to speed up the system response. The compensation of the large delays for low-Reynolds number applications is still an open problem and that is particularly relevant for flow control on membrane wings.

State-feedback and feed-forward control schemes in practical applications require estimations of the system response, which is usually done via low-order descriptions of the system. Some model reduction techniques have been previously used for high-Reynolds flows, including Volterra series [16] and Proper Orthogonal Decomposition (POD) [17]. Also for low Reynolds numbers flows around cylinders POD and the Eigensystem Realisation Algorithm (ERA) have been used [18, 19]. POD has also been previously adopted in the post-processing of the low Reynolds number flow around membrane wings [20], although actuation of the membrane has not yet been considered. POD-based ROMs have been successfully used for control-system design in several numerical and experimental investigations [21, 22, 23, 24].

This work aims to demonstrate a POD-based reduced-order description for integrally-actuated DE membrane wings to aid preliminary control feedback design. A previous work by the authors [12] has investigated the open-loop dynamics of actuated membrane wings in a low-Reynolds-number flow using a full-order coupled model. Further to those results, the same framework will be used in this paper to derive a suitable reduced-order model. Section II summarizes the full-order coupled aero-electromechanical model of Ref. [12]. Section III introduces two low-order description for the actuated membrane wing. By means of the two different reduced-order models (ROMs), section IV investigates the sensitivity of the identification method on the magnitude of the input signal and compares the results of the full and low-order description to assess the final results. Using the low-order description, PID and LQG controllers are designed (section IV.C) and finally implemented in the full-model to track required aerodynamic performance and compensate for disturbances of the inlet flow conditions (section IV.C.3).

II. High fidelity model

II.A. Electromechanical model

The structure is discretised using solid eight-noded, three-dimensional, hybrid elements with translational degrees of freedom [25]. The solution is based on a mixed formulation where the standard displacement-based description is augmented with an additional independent variable which describes the hydrostatic pressure. The new variable is coupled with the displacement solution through the constitutive model [25]. Considering the thickness of the membrane allows the definition of the electrostatic Maxwell stress tensor in all three-directions, relaxing the incompressibility assumption that would be otherwise required [12]. The hyperelastic constitutive model assumes a nearly-incompressible isotropic behaviour, with a voltage- and stretch-independent value of the dielectric constant. In particular, the constitutive material law is defined by the sum of a deviatoric, W_∞, and isochoric, U, free-energy functions. The deviatoric component will be described here by the Gent model [26], given as

$$W_\infty = -\frac{\mu J_m}{2} \log\left(1 - \frac{\bar{I}_1 - 3}{J_m}\right), \tag{1}$$

where μ and J_m are respectively the elastic shear modulus and limiting stretch constant, which are material dependent. The function is expressed in terms of $\bar{I}_1 = \mathrm{tr}\left(\bar{\boldsymbol{C}}\right)$, where $\bar{\boldsymbol{C}}$ is the right Cauchy-Green deviatoric deformation tensor, defined as $\bar{\boldsymbol{C}} = J^{-\frac{2}{3}}\boldsymbol{F}^T\boldsymbol{F}$, with $\boldsymbol{F}$ being the deformation gradient and $J = \det \boldsymbol{F}$ [27]. The volumetric part is defined as $U_\infty(J) = K(J-1)^2$, that is, a penalty function on the volume variation, where K is the compressibility modulus of the material. The mechanical stresses are then obtained as the work conjugates of the free energy function, $W = U_\infty + W_\infty$.

The constitutive model is completed by adding the effect of the electrostatic stresses, which are modelled here by means of the Maxwell's stress tensor. Given an electric field vector $\boldsymbol{E}$, the corresponding stress tensor $\boldsymbol{\sigma}_e$ is defined as [28]

$$\boldsymbol{\sigma}_e = \epsilon \boldsymbol{E} \otimes \boldsymbol{E} - \frac{1}{2}\epsilon \left(\boldsymbol{E} \cdot \boldsymbol{E}\right) \boldsymbol{I}, \tag{2}$$

where ϵ is the material dielectric constant, $\boldsymbol{E}$ is the electric field vector in the deformed coordinate system and $\boldsymbol{I}$ is the unitary second order tensor. The coefficients of this constitutive model are determined from experimental data on the specific material of interest. Buoso and Palacios [12] have obtained a good approximation to experimental results on an inflated VHB4905 membrane with μ= 20 kPa, J_m= 100, K= 3.8×10^8 Pa and $\epsilon = 2.7\epsilon_0$, where ϵ_0 is the in-vacuum dielectric constant.

II.B. Fluid model

Solutions to the low-Reynolds flow are obtained using a finite-volume discretization of the compressible Navier-Stokes equations with second-order-accurate integration in space and time. A low-Mach preconditioner is used to enhance convergence [29]. The solution of flow and energy equations is based on a coupled approach. No turbulence schemes or subgrid models were found necessary at the Reynolds number under investigation, Re = 2500. The membrane is modelled with a non-slip wall condition, and inlet, pressure outlet and free-stream boundary conditions are used for the boundaries of the fluid domain. In addition to studies on sensitivity to the grid-resolution and time step, for each case considered the element size and time step have been compared with the characteristic viscous length and time scales, that is, $l_\nu = \frac{\nu}{u_\nu}$ and $t_\nu = \frac{l_\nu}{u_\nu}$, respectively, where ν is the kinematic viscosity of the fluid and u_ν is the friction velocity [30]. The fluid mesh selected for the simulations in this work is well within this range, with a value of l^* and t^* below 3 throughout the domain.

II.C. Fluid-Structure coupling

The coupling of both solvers is based on the definition of a common interface occupying the same spatial position in both models. The pressure and viscous forces calculated in the fluid solver, are mapped using the shape function of the structural elements [29] into nodal loads for the finite-element (FE) solver. The new structural nodal displacements and velocities are then passed to the fluid solver for the deformation of the mesh and the computation of the new flow field. The mesh is deformed using 3D linear interpolation functions considering

the relative distance of the mesh nodes to the moving and fixed boundaries. The exchange of data between solvers uses a bridge in the RAM memory [29]. To capture the strong fluid-structure coupling between in membrane vibrations, an implicit coupling scheme between the structural and aerodynamic solvers has been used. The solution is initialised with a quasi-steady step, neglecting inertia forces and velocities of the membrane, and is then iterated with a dynamic step to converge to the real solution.

III. Model reduction

The full-order model described above is necessary to capture the problem physics, but its large cost is prohibitive in the context of control system design. Consequently, model reduction and system identification methodologies have been explored to establish the main parameters of the control system. The structural domain will be reduced using a projection into the system eigenvalues [31, 32]. Due to the large dimension of the coupled system, the reduced model for the fluid will be calculated using a Proper Orthogonal Decomposition (POD) [33, 34]. The time evolution of selected variables stored from a full-order simulation are used in the *snapshot method* for the calculation of the POD basis. The size of the basis is chosen by checking for convergence to the full-order solution and the percentage of the total energy retained (it is set to be greater than 99.5%) [35]. This has already been discussed in Buoso and Palacios [12], where it has also been shown that a few modes are enough to reconstruct the system dynamics over the relevant range of frequencies. POD has been preferred here to system identification techniques, such as ERA, for two reasons: i) the very slow natural frequencies of the system of the system would require much larger simulation times in an ERA; ii) "black-box" identification would not easily allow for a variation of the structural parameters in the structure or the introduction of non-linearities. This, as discussed below, is possible with POD basis. However, POD-based ROMs does not guarantee observability and controllability, and those had to be verified for all ROMs used in this work.

Such an approach does not rely on the availability of the discretisation matrices used

during the numerical integration of the full-order model, and can hence be applied to general purpose numerical frameworks as in the case of this work. Two reduced-order models (ROMs) of the fully-coupled system are then derived in now introduced. The main focus during the development of these tools is to investigate the cost/benefits of two approaches in terms of computational cost, robustness of the description and flexibility. Both ROMs are defined as SISO systems, with voltage and lift coefficient as time-dependent input and output, respectively. It is assumed a constant chordwise position of the membrane points, which was found to be a very good approximation in the flow conditions considered. The excitation of the system is done through a voltage input with fixed amplitude and a frequency sweep. While other excitations were explored [16, 36], this was seen to provide here a sufficient characterisation while reducing the computational cost.

The first ROM (section III.A) assumes that the system evolution can be described as a function of the structural degrees of freedom only. This defines a relatively simple approach with a very low computational cost associated to its identification. In the second model, described in section III.B, the fluid and structural dynamics are independently identified and then implicitly coupled to describe the full problem. This second model is more complex and substantially more computationally demanding, but provides a better characterisation of the system. In particular, while the structure-based description approximates well a given configuration, the second approach allows for changes in the electrode distribution.

III.A. Structure-based ROM

POD modes are identified from the wing out-of-plane displacements obtained from a full-order coupled simulation. A suitable excitation signal is needed as discussed above. The POD basis is used to define projection matrix $\mathbf{\Phi} \in \mathbb{R}^{m \times n}$, where m is the number of nodes of the structural domain and n is the number of basis selected. Displacements, velocities and acceleration histories are then projected into the modal matrix $\mathbf{\Phi}$ to compute the amplitudes $\mathbf{a}$, $\dot{\mathbf{a}}$ and $\ddot{\mathbf{a}}$ respectively. This reduces the aeroelastic system to a very low order linear

description of the form

$$\ddot{\mathbf{a}} + \mathbf{C}^*\dot{\mathbf{a}} + \mathbf{K}^*\mathbf{a} = \mathbf{G}^* V^2, \tag{3}$$

where $\mathbf{C}^*$ and $\mathbf{K}^*$ are the mass-normalised damping and stiffness matrices respectively defined in $\mathbb{R}^{n\times n}$, $\mathbf{G}^*$ is the mass-normalised gain matrix for the system input, defined in $\mathbb{R}^{n\times 1}$, and V is the known magnitude of the applied voltage. The only unknowns in Eq. (3) are the coefficients of the linear matrices. The equations are written as function of these coefficients for every simulation instant of the full-order model leading to a linear system of $3n^2$ unknowns. The system is then solved using a least-square approach, similar to the methodologies used in [37, 38]. It has to be noted that this methodology is substantially different from the Galerkin projection of the full-order matrices into the identified POD modes, but it has the advantage of not requiring access to the discretisation matrices of the full-order description, and can hence be used with general-purpose codes. This system is similar to the modal description of a membrane in vacuum but, in this case, the system matrices takes into account the effect of the surrounding fluid (albeit in a quasi-steady manner). The final system description, in a state-space formulation is

$$\dot{\mathbf{q}} = \begin{bmatrix} -\mathbf{C}^* & -\mathbf{K}^* \\ \mathbb{I} & \mathbf{0} \end{bmatrix} \mathbf{q} + \begin{bmatrix} \mathbf{G}^* \\ \mathbf{0}_v \end{bmatrix} V^2, \tag{4}$$

where $\mathbf{q} = \begin{Bmatrix} \dot{\mathbf{a}}(t)^\top & \mathbf{a}(t)^\top \end{Bmatrix}^\top \in \mathbb{R}^{2n\times 1}$, $\mathbb{I}$ and $\mathbf{0}$ are the unity and zeros matrices in $\mathbb{R}^{n\times n}$ and $\mathbf{0}_v$ is the zero vector of dimension $\mathbb{R}^{n\times 1}$. Eq. 4 defines a dynamical system describing the evolution of its states for a given input voltage. Once a reduced order description of the model has been satisfactorily obtained, the metric of the system performance has to be defined. Here it is the C_l which is approximated by a linear function of the states of the system and their evolution. and calculated as

$$C_l(t) = \mathbf{\Gamma} \begin{Bmatrix} \ddot{\mathbf{a}}(t)^\top & \dot{\mathbf{a}}(t)^\top & \mathbf{a}(t)^\top \end{Bmatrix}^\top, \tag{5}$$

where $\mathbf{\Gamma} \in \mathbb{R}^{1\times 3n}$ is determined imposing that (5) is satisfied in a least-square sense at every instant of the full-order simulation. This model can only represent the structural driven system response, and it assumes no internal dynamics in the fluid. However, it captures the main system dynamics at a low computational cost.

III.B. Aeroelastic ROM

In this second model, which will be used for the identification of the ROM and the control system design, the structural and fluid descriptions are individually identified and then coupled in a monolithic system. Similarly to the methods used by Thomas et al. [36] and Hall et al. [39], the fluid system is independently reduced considering its POD basis functions. However, while Thomas et al. [36] performed a series of full-order simulations on which a single structural mode was excited, the voltage input allows here for system excitations using a sweeping signal with a predefined frequency range. In this way multiple natural modes are excited at the same time, requiring only a single run (albeit a much more expensive one) of the coupled full-order model.

The reduced structural model is derived from the principle of virtual work for a 2D beam, but one in which the inertial, stiffness and actuation constants will be identified from the full-order model. It assumes, as before, constant chordwise position of the m points used for the discretisation of the 2D structure, zero bending stiffness and linear shape element functions. Linearising under these assumptions, the element mass, $\mathbf{M}_e$, stiffness, $\mathbf{K}_e$, and pressure load, $\mathbf{F}_e$, matrices are obtained and then assembled according to the standard procedure of the Finite Element Method. Since the membrane is made of DE, the structural model requires to take into account the effect of the voltage actuation into the stiffness matrix of the system. In fact, the actuation determines a relaxation of the membrane in-plane stress which, assuming incompressibility, is equal to $-\varepsilon\,(V/h_e)^2$ where ε is the material dielectric constant, V is the applied voltage and h_e the membrane thickness. The actuated element stiffness matrix $\mathbf{K}_e^V$

becomes then

$$\mathbf{K}_e^V = \frac{\sigma_0 h_e}{L_e}\begin{bmatrix} 1 & -1 \\ -1 & 1 \end{bmatrix} - \frac{\varepsilon V^2}{h_e L_e}\begin{bmatrix} 1 & -1 \\ -1 & 1 \end{bmatrix}. \tag{6}$$

The modal projection matrix $\mathbf{\Phi}_s$ is then calculated from the first n modal shapes of the structural system assuming a constant value of the applied voltage. The global mass, stiffness and pressure load matrices are projected into the reduced-subspace and the non-linear structural system assumes the form

$$\dot{\mathbf{q}}_s = \begin{bmatrix} \mathbf{0} & -\mathbf{M}_s^{-1}\mathbf{K}_s^V \\ \mathbb{I} & \mathbf{0} \end{bmatrix}\mathbf{q}_s + \begin{bmatrix} \mathbf{M}_s^{-1}\mathbf{F}_s \\ \mathbf{0} \end{bmatrix}\mathbf{a}_{ps}, \tag{7}$$

where $\mathbf{q}_s = \left\{\dot{\mathbf{a}}_s(t)^\top \quad \mathbf{a}_s(t)^\top\right\}^\top \in \mathbb{R}^{2n\times 1}$ is the vector of the structural modal amplitudes, $\mathbf{a}_s$, and their velocities, $\mathbf{M}_s$, $\mathbf{K}_s^V$, $\mathbf{F}_s$ are the modal mass, stiffness and pressure load $\mathbb{R}^{n\times n}$ matrices, respectively, and $\mathbf{a}_{ps}$ is the projection of the pressure difference distribution on the membrane defined in $\mathbb{R}^{n\times 1}$. In the specific, $\mathbf{K}_s^{NL}$ depends on the applied voltage V and it is obtained assembling the element matrices $\mathbf{K}_e^{NL}$ defined in Eq. (6) and projected into $\mathbf{\Phi}_s$.

In the linearised description used for linear control system design, the Maxwell stresses are defined as a system input through an electromechanical loading matrix, $\mathbf{\Psi}_e$. This will lead to a stiffer system than the original, but it is a necessary assumption to linearise the problem. For each membrane element, $\mathbf{\Psi}_e$ is then defined as

$$\mathbf{\Psi}_e = \frac{\varepsilon}{h_e L_e}\begin{bmatrix} y_{ei} & -y_{ei+1} \\ -y_{ei} & y_{ei+1} \end{bmatrix}, \tag{8}$$

where ε is the material dielectric constant and y_{ei} and y_{ei+1} are the vertical positions of the element nodes which, in the linearised description derived in this work, are assumed to be fixed at the values at the reference configuration considered. The linearised structural

equations are then of the form

$$\dot{\mathbf{q}}_s = \begin{bmatrix} \mathbf{0} & -\mathbf{M}_s^{-1}\mathbf{K}_s \\ \mathbb{I} & \mathbf{0} \end{bmatrix} \mathbf{q}_s + \begin{bmatrix} \mathbf{M}_s^{-1}\mathbf{\Psi}_s \\ \mathbf{0} \end{bmatrix} \boldsymbol{\theta}_s V^2 + \begin{bmatrix} \mathbf{M}_s^{-1}\mathbf{F}_s \\ \mathbf{0} \end{bmatrix} \mathbf{a}_{ps}, \tag{9}$$

where $\mathbf{q}_s = \left\{ \dot{\mathbf{a}}_s(t)^\top \quad \mathbf{a}_s(t)^\top \right\}^\top \in \mathbb{R}^{2n\times 1}$ is the vector of the structural modal amplitudes, $\mathbf{a}_s$, and their velocities, $\dot{\mathbf{a}}_s$, $\mathbf{M}_s$, $\mathbf{K}_s$, $\mathbf{F}_s$ and $\mathbf{\Psi}_s$ are the modal mass, stiffness, pressure load and electromechanical matrices, respectively, and $\mathbf{a}_{ps}$ is the projection of the pressure difference distribution on the membrane. In Eq. (9), $\theta_{s,i} = \Phi^T_{s,ij}\theta_j$ represents the projection of the voltage distribution on the membrane with θ_j being equal to one if the voltage is applied on the j-th node, or zero otherwise. Unless specifically stated, in this work it is assumed an integral membrane actuation setting all the components θ_j equal to one.

The flow field is characterised as a first-order system in the amplitudes of the POD modes. The dominant POD modes are identified using the pressure evolution on the membrane surface only. As it will be seen in section IV.B, this provides comparable fidelity for aeroelastic analysis to that provided by PODs based on the pressure field in the entire fluid domain, but at a fraction of the cost. The identified basis are used to build the projection matrix $\mathbf{\Phi}_f$ with k selected modes. The number of structural and fluid modes are the same, $k = n$. The value selected for k and n is the minimum number of basis which satisfied the energy criteria of the POD. The pressure history is projected to obtain the corresponding modal amplitudes, $\mathbf{a}_p$. The structural displacements, velocities and accelerations from the same full-order simulation are projected into a modal subspace defined by the membrane modal shapes in vacuum, which has been defined as $\mathbf{\Phi}_s$, obtaining $\mathbf{a}_s$, $\dot{\mathbf{a}}_s$ and $\ddot{\mathbf{a}}_s$ respectively. The fluid model is finally defined as

$$\dot{\boldsymbol{a}}_{pf} = \mathbf{A}_p \boldsymbol{a}_{pf} + \mathbf{B}_a \ddot{\boldsymbol{a}}_s + \mathbf{C}_v \dot{\boldsymbol{a}}_s + \mathbf{D}_d \boldsymbol{a}_s \tag{10}$$

where $\mathbf{A}_p \in \mathbb{R}^{n\times n}$ is the matrix representing the fluid dynamics, and $\mathbf{B}_a, \mathbf{C}_v$ and $\mathbf{D}_d$ are the

$\mathbb{R}^{n\times n}$ matrices describing the evolution of the boundary conditions due to the membrane deformation. They are obtained imposing that (10) is satisfied for the training data in a least-square sense at every instant for all system states. Using the fact that $\boldsymbol{a}_{ps} = \boldsymbol{\Phi}_s^T \boldsymbol{\Phi}_f \boldsymbol{a}_{pf}$, Eq. (9) and (10) are coupled in a monolithic system of the form

$$\dot{\mathbf{q}} = \boldsymbol{\Omega}\mathbf{q} + \boldsymbol{\Sigma} V^2 \tag{11}$$

where $\mathbf{q} = \begin{Bmatrix} \dot{\mathbf{a}}_s(t)^\top & \mathbf{a}_s(t)^\top & \mathbf{a}_{pf}(t)^\top \end{Bmatrix}^\top \in \mathbb{R}^{3n\times 1}$, and the matrices $\boldsymbol{\Omega}$ and $\boldsymbol{\Sigma}$ are defined as

$$\boldsymbol{\Omega} = \begin{bmatrix} \mathbf{0} & -\mathbf{M}_s^{-1}\mathbf{K}_s & \mathbf{M}_s^{-1}\mathbf{F}_s\boldsymbol{\Phi}_s^T\boldsymbol{\Phi}_f \\ \mathbb{I} & \mathbf{0} & \mathbf{0} \\ \mathbf{C}_v & \mathbf{D}_d - \mathbf{B}_a\mathbf{M}_s^{-1}\mathbf{K}_s & \mathbf{A}_p + \mathbf{B}_a\mathbf{M}_s^{-1}\mathbf{F}_s\boldsymbol{\Phi}_s^T\boldsymbol{\Phi}_f \end{bmatrix}, \quad \boldsymbol{\Sigma} = \begin{bmatrix} \mathbf{M}_s^{-1}\boldsymbol{\Psi}_s \\ \mathbf{0} \\ \mathbf{B}_a\mathbf{M}_s^{-1}\boldsymbol{\Psi}_s \end{bmatrix} \boldsymbol{\theta}_s. \tag{12}$$

In this case, the availability of the pressure distribution during the integration allows the direct computation of the lift coefficient which, after linearisation, can be obtained as a linear combination of the system states $\boldsymbol{a}_s$ and $\boldsymbol{a}_{pf}$. As compared to the Structure-based ROM of section III.A, the Aeroelastic ROM introduces an additional level of complexity, related to the individual reduction and implicit coupling of the fluid and structural descriptions. This gives a more complete description of the problem since it approximates the pressure distribution along the membrane, which allows the investigation of the number and location of system outputs (pressure measurements) in control design. Additionally, it allows for the independent modification of only one of the two models, which is particularly useful to investigate actuation strategies such as the initial prestretch or the extension of the electrodes on the wing surface. As a drawback, the Aeroelastic ROM requires the post-processing of a larger amount of data for its identification.

The coupling of the separated flow and the highly-deformable membrane will be strongly non-linear, adn therefore the system response will depend on the amplitude of the inputs (in particular, the actuation voltage). These non-linearities can not be fully captured in

the ROMs, due to the modelling simplifications for their derivation, and the effect of the amplitude of the excitation signal needs to be investigated before the identification of the Aeroelastic ROM.

IV. Numerical results

The model reduction methodology described above will be exercise now on a numerical example and used for the design of a controller for gust alleviation. Section IV.A investigates the effect of the amplitude of the input signal used for the system identification, using the Structure-based ROM of section III.A. This allows to limit the computational cost of this parametric study on the amplitude of the training signal. Then, a reduced-order model is identified using the Aeroelastic ROM described in section III.B and compared to the full-order model in section IV.B. Next, in section IV.C the Aeroelastic ROM is used to design PID and LQG control schemes and evaluate their tracking and gust rejection performance. The controllers are finally implemented in the full-order model in section IV.C.3 and their performance is compared with the predictions of the ROM-based closed-loop transfer functions. All results are non-dimensionalized by the chord length c and flow velocity V_∞. In particular, the evolution histories of the structure and aerodynamic coefficients are presented as function of the non-dimensional time $t^* = tV_\infty/c$ and the frequencies are expressed in term of the Strouhal number $\mathrm{St} = fc/V_\infty$.

The reference case is a 2D membrane on rigid supports in the presence of a fluid with Reynolds number $\mathrm{Re} = 2500$, free-stream velocity $V_\infty = 1.445$ m/s and angle of attack $\alpha = 4°$. These flow conditions have been considered in a verification exercise in a previous work from the authors [12], and are therefore used here for this initial investigation on model reduction and control design. A schematic representation of the problem is shown in Fig. 1 together with a zoom on the wing.

The membrane has a chord $c = 30$ mm and an initial thickness $h = 0.05$ mm for a prestretch $\lambda_p = 1.02$, which determines a highly compliant case. In this work the prestretch

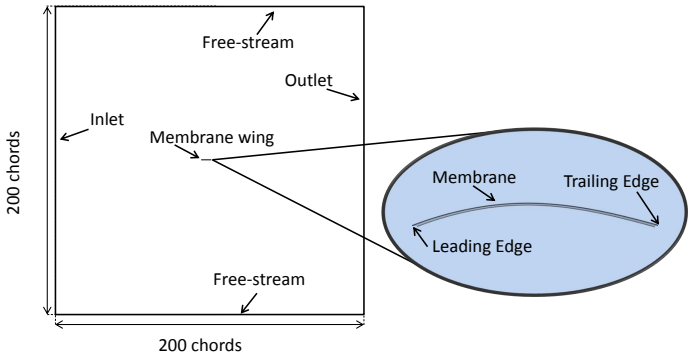

Figure 1: Aeroelastic model.

λ_p refers to the ratio between the prestretched and undeformed membrane length. The membrane is pinned at the lower side of the leading and trailing edge. The structure is discretised with 800 elements chordwise, and one element in the thickness direction. Since a 2D problem is addressed, a single element is used in the spanwise direction as well. Mesh refinement and time-step sensitivity studies have been conducted in dynamic simulations for an angle of attack $\alpha = 8°$, at which self-excited oscillations are observed in the system due to the shedding of vortices from the leading edge. The relative errors on the mean value of C_l as well as the amplitudes and frequencies of its oscillations were considered to establish convergence. The maximum relative error of those quantities was set at 5%. The sensitivity study considering this conditions allows to identify a suitable spatial and temporal resolution to capture this coherent structures intrinsically related to the fluid internal dynamics. The resulting mesh size and time-step were found to be enough to properly capture the dynamics of the actuated cases at lower angles of attack. The resulting fluid domain extends for 100 chords in both directions and it is meshed with one million elements, which corresponds to 400 elements along the membrane walls in the chordwise direction, 400 in the flow direction for the wake, and 400 elements in the radial directions from the chord. The smallest element at the membrane wall is 50 μm and the biggest elements, at the domain boundaries, are around twice the size of the membrane chord. The reference case is characterised by a maximum amplitude $y^* = y/c = 0.02$ at $x/c = 0.43$. The lift coefficient is $C_l = 0.47$.

IV.A. ROM based on structural information and dependency of amplitude

As mentioned above, the expected strong non-linear response of the fully-coupled system requires the investigation of the dependence of its dynamics with the amplitude of the actuation voltage. Varying the input signal can in fact enhance different physical effects that will determine more or less substantial differences in the identified ROMs. The system is excited with a uniform harmonic voltage of the form $V = V_0 \sin(2\pi \mathrm{St}_v t^*)$, where V_0 is the voltage amplitude and St_v is the non-dimensional actuation frequency, $\mathrm{St}_v = f_v c/V_\infty$. The amplitudes considered are $V_0 = 150$, 250 and 500 V. In all three cases the frequency St_v is varying linearly from 0 to 0.4 in a time window of $T^* = 90$. The effective reduced frequency content of the output spans from 0 to 1.6 because the system is excited by the resulting Maxwell stress, which evolves at twice the voltage frequency. Increasing the amplitude of the input signal determines a higher mean value of the Maxwell stress responsible for the membrane tension relaxation. This leads to a reduction of the system resonant frequencies, to larger mean camber and structural oscillations and to an increase of the effect of structural and fluid non-linearities in the system response. The ROM is trained over the entire simulation time, $T^* = 90$, and data are collected every $\Delta t^* = 0.02$. In this investigation only the structural degrees of freedom are considered, and the lift coefficient is takes as performance metric of the system response. The data stored then will allow the identification of the reduced order description using the model of section III.A.

For each of the three cases the first four POD modes are shown in Fig. 2a while Fig. 2b quantifies their cumulative contribution to the total system energy. For all three cases the minimum energy represented by the retained modes has been set to 99.95%, leading to the choice of 3 modes for $V_0 = 150$ V and 250 V, and 5 modes for $V_0 = 500$ V. In the first two cases, the first membrane mode has the largest contribution to the system evolution (Fig. 2b), with minor effects from the second and third modes. In addition, the spatial modes are very similar in shape for the first two signals, and their amplitudes are proportional to the square ratio of the applied voltages $\left(\frac{V_{02}}{V_{01}}\right)^2$, demonstrating weak non-linearities of the problem. For $V_0 = 500$ V, the first and second modes have a similar contribution to the

response, and secondary contributions can be observed for modes three to five. The different mode shapes show that the system start exhibiting some fluid and structural non-linearities, which translates in the higher number of modes needed for its description. Ref. [12] has also investigated the number of POD modes required to reconstruct the C_l evolution of the system. It was found, in agreement with the results here, that two modes were enough to reconstruct the signal at the frequencies of interest.

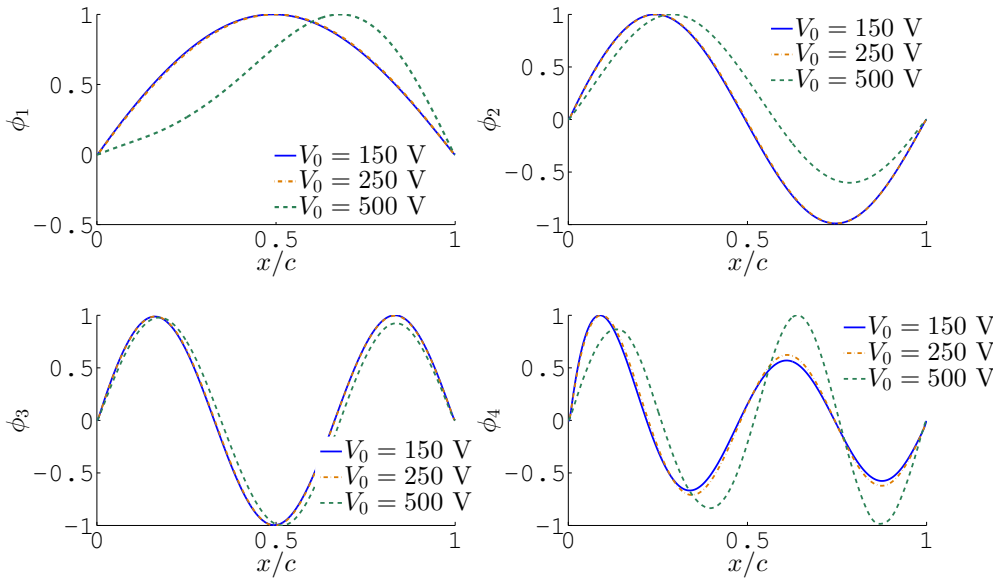

(a) Modal shapes.

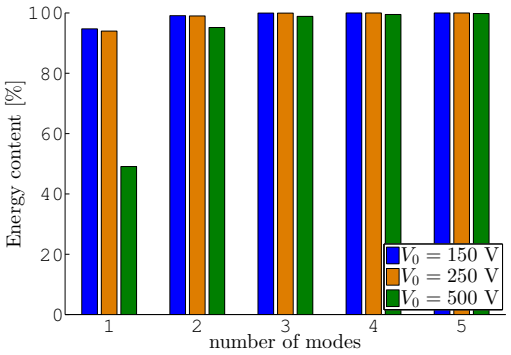

(b) Total energy retained.

Figure 2: POD modal bases for the excitation cases with $V_0 = 150$, 250 and 500 V and their contribution to the total system energy.

The resulting dynamical systems obtained from the identification are compared in Fig. 3, which shows the transfer functions of the membrane C_l for a harmonic actuation input Φ. For

an applied voltage $V = V_0 \sin(2\pi \mathrm{St}_v t^*)$ the system will react to $V^2 = \frac{V_0^2}{2} - \frac{V_0^2}{2}\cos(2\pi 2\mathrm{St}_v t^*)$ which is proportional to the Maxwell stress on the DE. The reduced frequency considered in Fig. 3 refers to the effective forcing frequency, and hence to twice the one of the applied voltage. The resulting time-dependent function of the Maxwell stress will be denoted with Φ. The non-dimensional natural frequencies, St, and damping ratios, ξ, of the three ROMs are shown in Table 1. The impact of the mean actuation voltage in the signal used for the system identification is clear: a higher amplitude causes a shift of the resonances of the system to lower frequencies and increases the peak amplitude. This becomes more important towards higher frequencies, due to the coupling with the flow. For $V_0 = 500$, the transfer function shows some differences as compared to the other two cases, with a slightly damped peak at $\mathrm{St} = 0.75$. This shows that higher frequencies are less damped in the coupled problem. The lower damping of the higher modes as compared to the first one is the indication that these are most likely to be excited by the coupling with the flow. These numerical results are in agreement with the experimental work by Arbos-Torrent et al. [2] and Rojratsirikul et al. [40], who observed the predominance of the second and higher system modes in the dynamic response of membrane wings. They also found that the first membrane mode was found to be dominant when large structural observation were measured, suggesting its impact in structural-driven system dynamics.

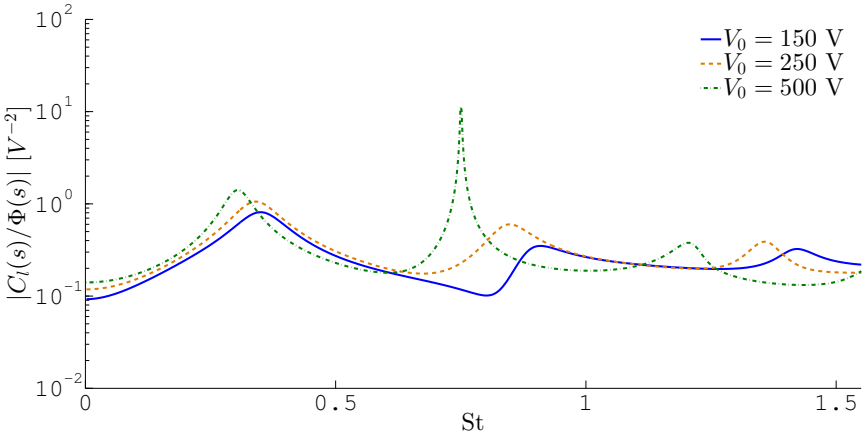

Figure 3: C_l transfer functions for the three different ROMs with Φ in 10^{12} V^2.

Comparison of the dynamical systems obtained with different system excitations shows

Table 1: Resonant frequencies and damping of the identified linear systems

$\mathbf{V_0}$ [V]	**Mode 1**		**Mode 2**		**Mode 3**	
	St	ξ	St	ξ	St	ξ
150	0.35	5.53	0.88	2.03	1.42	1.02
250	0.34	5.15	0.84	2.04	1.36	1.15
500	0.30	3.48	0.75	0.07	1.21	1.04

that in all three cases similar features have been identified. The reduced-order model used for control design in section IV.B will be obtained with a voltage amplitude of $V_0 = 250$ V.

IV.B. Reduced-order model identification

The simple reduced-order description of section III.A has shown to be useful for a preliminary investigation on the input signal required for the system identification, but for control design a more accurate description of the full system is required, such as that offered by the Aeroelastic ROM of section III.B. It also allows to consider different electrode layouts by the selection of the non-zero entries of the voltage distribution vector in Eq. (9). For the identification of the ROM, the full wing is excited with the same voltage signal described in section IV.A and an amplitude of $V_0 = 250$V. Two modes for both the fluid and the structure were found to satisfy the POD criteria for the reconstruction of the system dynamics. For the identification of the reduced-order model of the fluid, the POD has been applied to the evolution of the pressure distribution on the membrane. Despite the reduced set of data considered, the POD applied to the pressure distribution on the wing was seen to represent the same basic system dynamics as a full-domain POD, with a much smaller computational cost. The transfer functions of the pressure evolution on the membrane from actuation obtained in the two cases were in fact nearly identical, but those results have not been included here for brevity.

The lift coefficient predicted by the Aeroelastic ROM is then compared with the full model to assess its suitability to describe the full system dynamics. Fig. 4 shows the C_l for

different input voltages for the full-order model and the linearised version of the ROM. From these results, the Aeroelastic ROM used later in this work will be obtained using a training signal at amplitude $V_0 = 250$V and the sweeping frequencies described in the previous section. Overall, the good agreement of full and reduced-order models demonstrates that this ROM is able to capture the main system dynamics. While each run of the full-order model requires approximatively 24 hours on 16 CPUs to provide sufficient data points for training the ROM, the ROM itself runs in seconds on a single CPU.

As discussed in Ref. [12], this system size is sufficient to reconstruct the relevant time histories and the small discrepancies are related to the modelling assumptions of the linear models. In particular, the low-order model predicts a stiffer membrane behaviour which results in a reduced C_l amplitude and a shift of the system resonance towards higher frequencies. As discussed in section III.B, this was expected from the linearisation approach used for the Maxwell stresses. The difference is similar in both cases shown in Fig. 4, which suggests that this discrepancy could be mitigated during the control system design by reducing the control system gains before the implementation in the full-order model. For large frequencies, the system performance are mainly defined by the forcing effect of the structure. The small differences at the lowest actuation frequencies in Fig. 4b have been related to the non-linear coupling of the systems, which can not been captured in a linear description. This is exemplified in Fig. 5 which shows the C_l evolution for an integral voltage actuation with amplitude $V_0 = 250$ V and frequency $\mathrm{St}_v = 0.08$. The plot compares the performance prediction of the full model, the linear Aeroelastic ROM described in section III.B and the non-linear ROM obtained updating the stiffness matrix at each time step according to Eq. (6). This non-linear ROM does not require a new training procedure. It is in fact based on the Aeroelastic ROM with the modification of the stiffness matrix at every time step. This highlights, once again, the flexibility and robustness of the model-reduction methodology considered. The introduction of the non-linear structural component in the system description gives an even better agreement with the full-order model. Nevertheless, the linear model can still offer a satisfactory representation of the system performance to build a

control system.

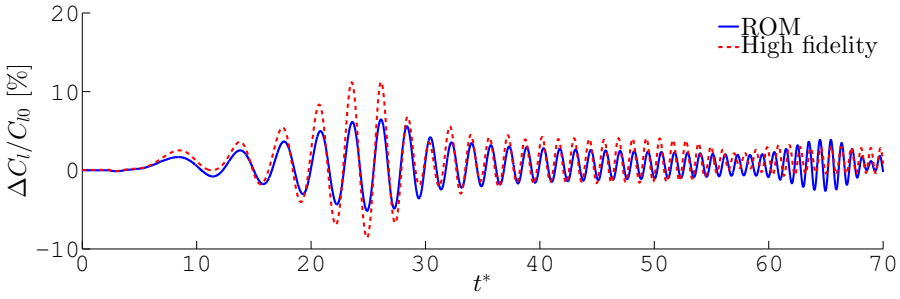

(a) $V_0 = 150$ V.

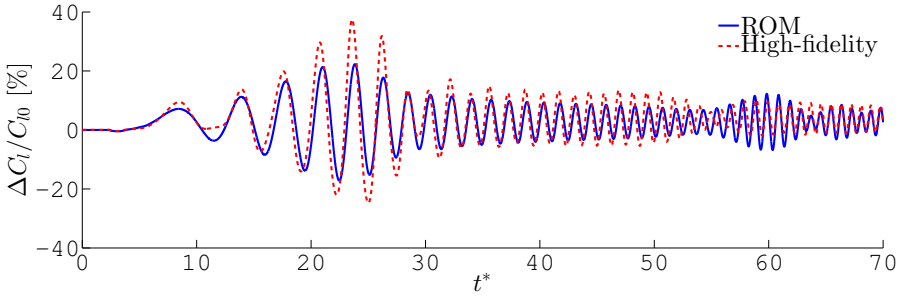

(b) $V_0 = 250$ V.

Figure 4: Comparison of the full and reduced-order descriptions: C_l evolution for an input voltage $V = V_0 \sin(2\pi \mathrm{St}_v t^*)$ with St_v linearly varying from 0 to 0.3, a) $V_0 = 150$ V and a) $V_0 = 250$ V.

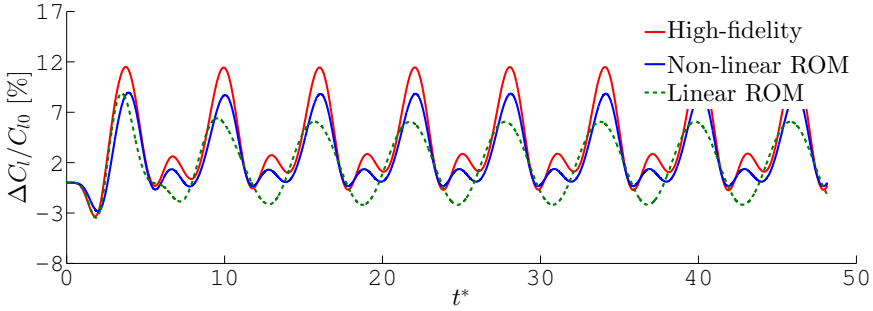

Figure 5: C_l evolution for an integral actuation with an input voltage $V = V_0 \sin(2\pi \mathrm{St}_v t^*)$ with $V_0 = 250$ V and $\mathrm{St}_v = 0.08$. Comparison of the performance from the full-order model, non-linear and linear ROMs.

To demonstrate even further the flexibility of the reduced-order model approach of this work, it is now considered a different case, with an electrode extending only on the first

half of the aerofoil. It uses the same Aeroelastic ROM as before, identified via the sweeping voltage signal, but the effect of the actuation voltage is prescribed only on the first half of the wing, modifying the electrodes distribution vector $\boldsymbol{\theta}$ in Eq. (8) . Fig. 6 compares the C_l evolutions in the full-order simulation and the non-linear ROM. The low order-description slightly overestimates the oscillations of the lift coefficient, but adequately captures both the main system dynamics and the C_l evolution close to its minimum values.

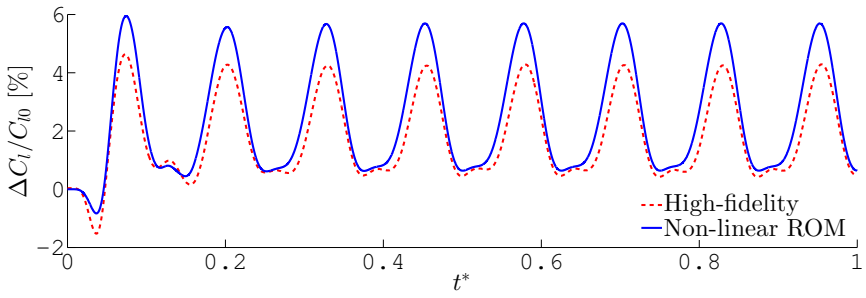

Figure 6: C_l evolution with half-chord electrode and input voltage $V = V_0 \sin(2\pi \mathrm{St}_v t^*)$ with $V_0 = 250$ V and $\mathrm{St}_v = 0.08$. Results from the full-order and non-linear low-order models.

Note finally the significant system delays of the actuated system. Fig. 7 presents the C_l variation over the mean value for the input signal used for the system identification. Comparing the time evolutions of the input and output signals it is evident the large lag of the system response which is related to the fluid convective time-scale [7, 14]. Williams et al. [15], who considered an actuated wing in a low-Reynolds-number flow, have also identified large delays in the actuated system, and the limits that this imposes on the effectiveness of feedback controllers.

IV.C. Control system design

Two common control architectures, a PID-type controller and a Linear Quadratic Gaussian (LQG) regulator, will be investigated to track a prescribed lift evolution and reject flow disturbances. It has to be noted that the actuation through DEs in the specific configuration considered is characterised by a zero-saturation: the controller effort depends on V^2 which only allows for the relaxation of the membrane tension. This is a constraint which could

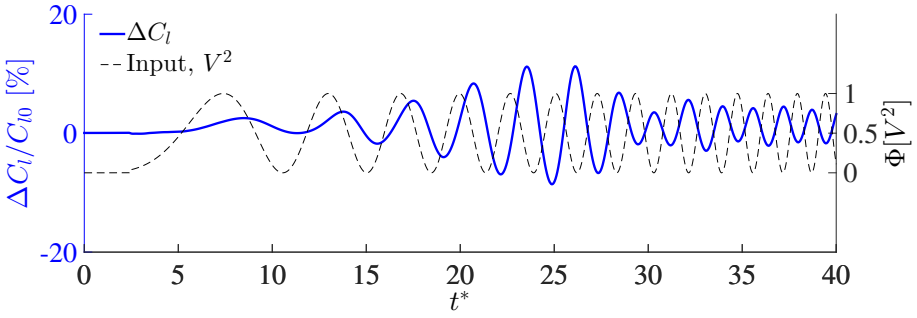

Figure 7: Input ($\Phi(s) = V^2(s)$) and output (C_l) signals in the training process used for identification ($V_0 = 250$ V).

be mitigated with a different actuator design, but this is beyond the scope of the present work. Additionally, the design of the control system will focus on reduced frequencies up to St $= 0.1$ that have been estimated to be the upper limit for the atmospheric disturbances expected for MAVs applications [7].

IV.C.1. Proportional-Integral-Derivative (PID) controller

A PID controller for a SISO system is defined as

$$V^2(t) = K_i \int_0^t e(\tau)d\tau + K_p e(t) + K_d \dot{e}(t), \tag{13}$$

where V is the applied voltage, K_i, K_p and K_d are the integral, proportional and derivative gains, and $e(t) = C_{l,ref} - C_l(t)$ is the instantaneous error with the reference lift coefficient, $C_{l,ref}$. The gains are designed using the reduced-order model by investigating the transfer function of its closed loop response. Fig. 8 shows the magnitude and phase of the transfer functions in the tracking problem, H_1, and in the rejection of flow disturbances, H_2. The figures also show the dependence of the closed-loop performance on the integral gain.

Considering the tracking performance, larger values of K_i determine amplitudes of H_1 closer to unity for wider ranges of reduced frequencies. The phase of the tracking transfer function shows significant lag, resulting in poor tracking performance of fast time-dependent signals. The integral gain can be augmented up to a maximum value (grey line) that leads

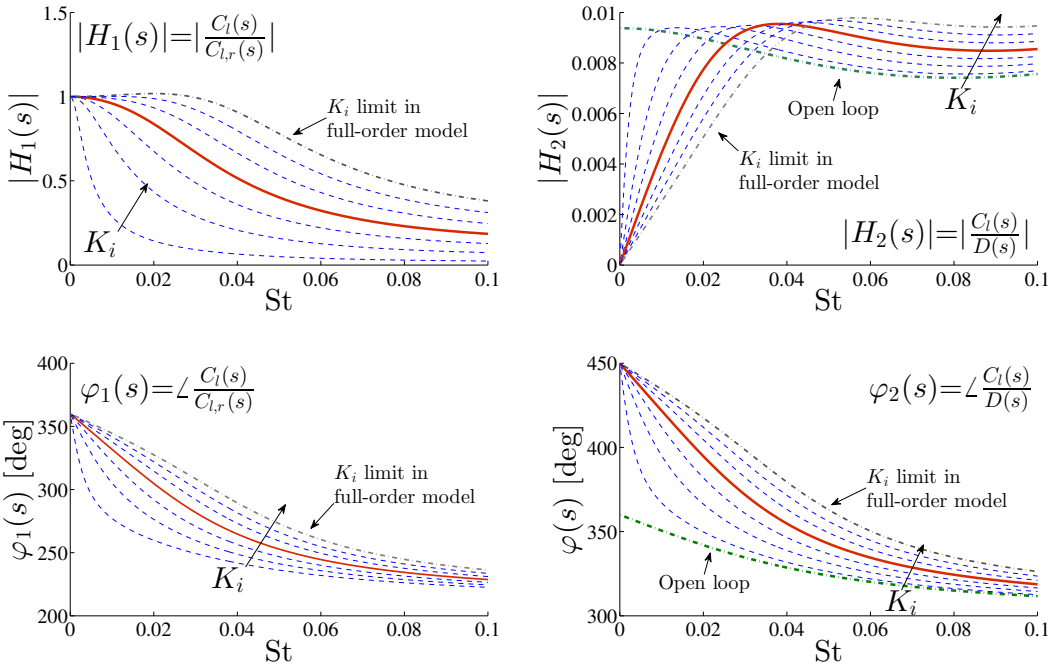

Figure 8: Closed-loop transfer functions with PID control architecture: influence of integral gain K_i on tracking performance and sensitivity to flow disturbances.

to the system destabilisation in the full-order description. This has been found by the evaluation of the controller performance in the full-order model. It is also observed that, for values of K_i above $8{\times}10^{15}\ V^2/s$ (continuous line in Fig. 8), the magnitude of H_1 is greater than one for a small frequency bandwidth and it results in an overshoot of the tracking performance for a step input in both reduced and full-order models. When considering the sensitivity to disturbances, it is observed a higher rejection at low frequencies for larger values of K_i. It is seen, in fact, that the amplitude of the C_l oscillations meets the one of the open-loop case (also shown in Fig. 8) at higher St numbers for large values of K_i, increasing the bandwidth of the effectiveness of the controller. The effectiveness is measured as the reduction of the amplitudes of the oscillations as compared to the open-loop case. However, after intersecting the open-loop transfer function, higher values of K_i determines larger amplification of the disturbances. Based on these considerations, the value of the K_i controller selected is $K_i = 8 \times 10^{15}\ V^2/s$ in order to avoid the overshooting of the step response during tracking. This limits the bandwidth of effectiveness in disturbance rejection

to St = 0.03. It has also been found that the augmentation of the PI gains lead to the destabilisation of the aeroelastic system. Thus, it is set $K_d = 0$ and $K_p = 5.4 \times 10^{13}\ V^2$. The integral gain has been set to $K_i = 8.0 \times 10^{15}\ V^2/s$.

IV.C.2. Linear Quadratic Gaussian (LQG) controller

In the LQG feedback scheme the controller action is proportional to an estimate of the system states through a constant gain matrix [41]. The matrix is obtained as the solution of the Algebraic Riccati equation which minimises the cost function

$$J = \int_0^\infty \left(\boldsymbol{x}^T \boldsymbol{Q} \boldsymbol{x} + Q_i e^2 + u^2 \right) dt, \tag{14}$$

where $\boldsymbol{x}$ are the states of the Aeroelastic ROM, e the lift tracking error, $\boldsymbol{Q}$ and Q_i are the weights of the aeroelastic states and of the tracking error, respectively, and u is the normalised voltage input defined as $u = V/V_{max}$ where $V_{max} = 500V$ is the maximum actuation voltage, which is within the limits of validity of the electromechanical material model. The diagonal components of the weight matrix, $\boldsymbol{Q}$, are initially estimated based on the maximum amplitudes of the modes obtained during the full-order simulations. Only diagonal entries are considered for $\boldsymbol{Q}$. The controller relies on structural oscillations for the compensation of the lift coefficient through a variation of the membrane camber with the actuation. This implies that very small weights are given to the structural degrees of freedom (the modal amplitudes and their derivatives), to allow for the large variations required to compensate for changes in the lift. The selection of the gains for the amplitude of the pressure modes and the servo-component are selected based on a parametric study on the closed-loop performance of the reduced-order model.

The states of the system are not available in the full-order description, and need to be estimated in real-time for the implementation of the state-feedback scheme using a Kalman filter [41]. The design of the Kalman filter is done by setting to zero the noise cross-correlation matrix and varying the ratio of the correlation matrices of input and measurement noise. In

the current design it is assumed minimal noise in the output measurement, so the ratio is set to 10^5. The design of the Kalman filter has been verified for an open and closed-loop conditions in the full-order model and showed to predict well both the system states and the lift coefficient.

For the tracking problem, an additional integral weight, Q_i, is used to correct for the error between the current and the reference lift signals. This defines an outer control loop whose commands are added to the LQG actions. Fig. 9 shows the magnitude and phase of the transfer functions to track a reference lift, H_1, and to reject flow disturbances, H_2, as function of the selected integral weight. In the case proposed here, Q_i is varied in the range between $0.6\times10^{10} - 1.6\times10^{10}$ with a 0.2×10^{10} step increase. Lower values have shown very poor tracking performance also for constant tracking signals, and have therefore not been included in the results. The weights of the structural states and their derivatives are set to 1, and the pressure weights to 1×10^2 and 1.2×10^2 for the first and second mode respectively. The parametric study shows that increasing the integral gain leads to overall better tracking performance. This trend continues up to an upper bound, indicated in the figure, where the controller destabilises the full-order system, $Q_i = 1.6 \times 10^{10}$. Increasing Q_i also helps in the rejection of disturbances at low frequencies. However, high-frequency oscillations are amplified by the controller. The selected gain $Q_i = 1.0 \times 10^{10}$ (continuous line in Fig. 9) has its higher frequency of disturbance rejection at St = 0.04.

A similar exercise has been carried on for the variation of the weights of the states related to the pressure evolution, but it is not shown here for conciseness. The main results is that the increase of these weights has the opposite effect of the increase of Q_i. The final design has been selected to reduce the tracking time of a step response while still maintaining satisfactory gust rejection performance at low Strouhal numbers.

IV.C.3. Implementation of the controllers in the full-order model

Section IV.B has already demonstrated the agreement of the full-order and reduced-order models, and the robustness and flexibility of the Aeroelastic ROM. Here the controllers

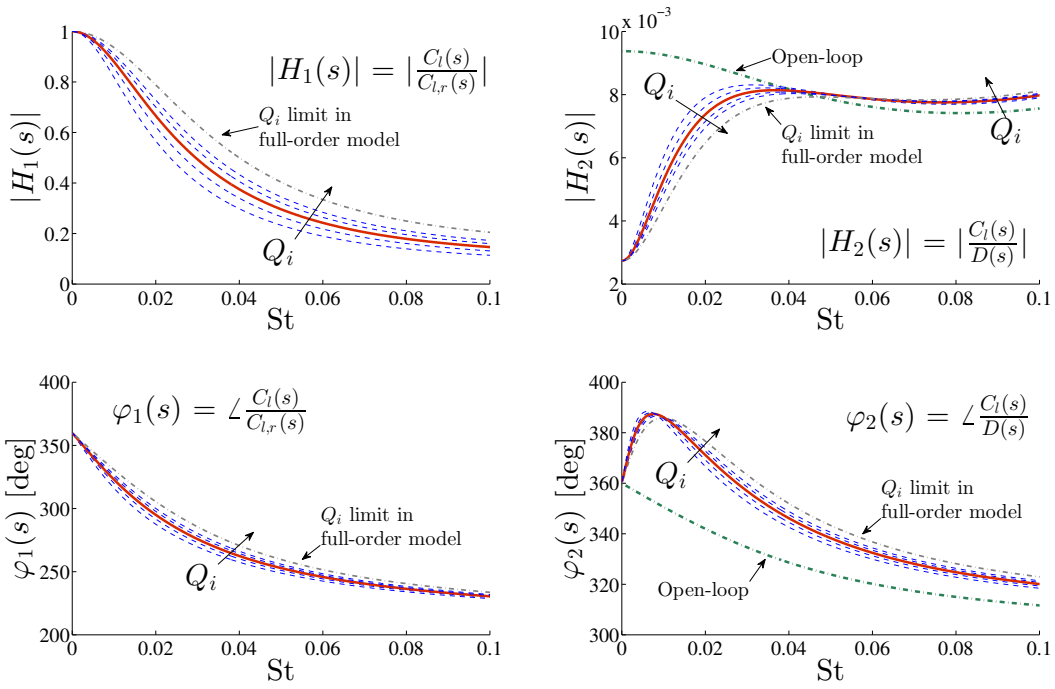

Figure 9: Closed-loop transfer functions with LQG control architecture: influence of the weight of the integral component Q_i on tracking performance and sensitivity to flow disturbances.

obtained using the ROMs in the previous section will be exercised in a simulation of the closed-loop membrane response using the high-fidelity model.

First, the closed-loop performance in the full-order model is evaluated in the tracking of a step change in the reference lift. The PID and LQG controllers are required to track an increase of 5% of the reference lift coefficient, $C_{l,ref}$. Fig. 10 shows the evolution of the lift and the applied voltage in the closed-loop systems defined by the PID and LQG controllers. The actuation voltage determines a relaxation of the membrane tension and an increase in the camber that leads to the required increase in lift. Both controllers show similar system response, with the chosen PID law being a more aggressive tracking strategy. This is simply due to the selection of gains in the control design process. Results in Fig. 10 are compared to the step response in open loop, which shows strong oscillations at the frequency of the first aeroelastic mode. Those are still present, but with smaller amplitudes, in the closed-loop response. They are related to the initial conditions and are too fast be controlled by the

present feedback schemes, as it was seen in Fig. 9.

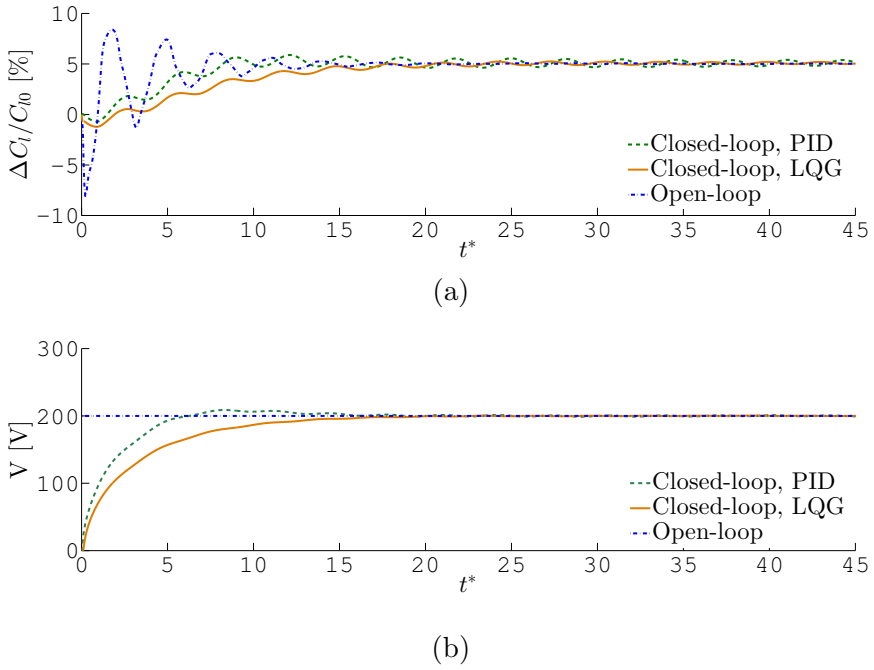

Figure 10: Step responses for the open-loop and closed-loop systems in the full-order model: a) C_l history and b) voltage requirements.

The analysis of the tracking performance of Fig. 8 and Fig. 9 highlighted a degradation of the tracking performance with time-dependent signals of increasing reduced frequency. This is verified in the full-order model considering the tracking of a reference signal, $C_{l,ref}$, of the form

$$C_{l,ref} = C_{l0}(1 + \delta C_l)\left[1 - \cos\left(2\pi \mathrm{St}_{C_l} t^*\right)\right] \tag{15}$$

where δC_l and St_{Cl} are the amplitude and frequency of the oscillations. The investigation is shown here only for the LQG controller, but similar results were obtained for the PID case. Fig. 11 shows the C_l evolution and the controller effort for the the LQG control scheme in the full-order model. The plots considers two cases with $\delta C_l = 2.5\%$ and $\mathrm{St}_{C_l} = 0.02$ and 0.04. In the plots, $C_{l,ref}$ refers to the reference signal to be tracked, while the full-order model and ROM to the resulting C_l of the closed-loop response in the full-order and ROM, respectively. A very good agreement is found between the two models showing the capability of the ROM to reproduce the system behaviour with a good fidelity. In addition, as highlighted from the

parametric study of Fig. 9, the physical system exhibits a phase delay which increases with the frequency of the excitation, thus reducing the effectiveness of the control law. Also, when increasing the frequency of the reference signal, there is a reduction of the amplitude gain, in agreement with what predicted by the closed-loop transfer function of the Aeroelastic ROM. The plots show that the controller is actuating the wing with a positive voltage, resulting in a relaxation of the membrane tension, an increase in the camber and a resulting increase in the lift coefficient. As it can be seen from the time histories of lift and voltage, both delays are identified and their combined effect determines the upper frequency of the closed-loop system. The first delay is due to the control system architecture, and can be identified between the lags of the peaks in the reference signal and the voltage amplitude. The second effect is evident when considering the time delay between the maximum peak of the voltage and the corresponding peak in the C_l. The identification of these delays is consistent with previous experimental investigation in the literature [7, 15].

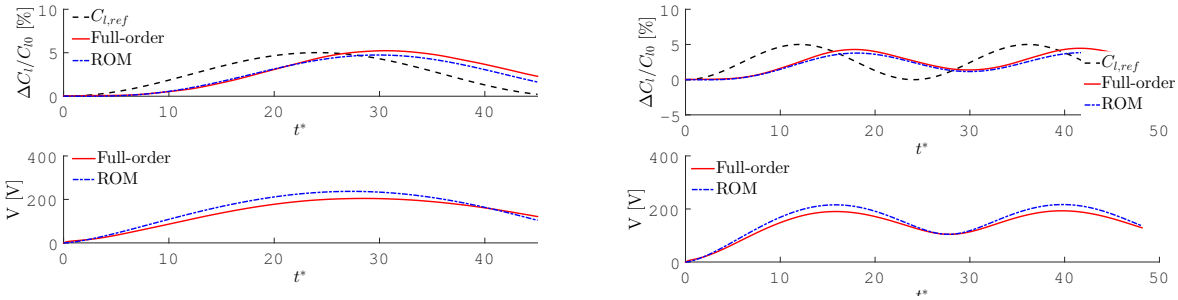

(a) $\mathrm{St}_{C_l} = 0.02$. (b) $\mathrm{St}_{C_l} = 0.04$.

Figure 11: Tracking of sinusoidal lift. Comparison of the performance from the full and reduced-order models for a LQG state-feedback control scheme.

The closed-loop performance of the wing is finally investigated under flow disturbances. This has the double aim of comparing the prediction of the closed-loop transfer function with the full-order model and show the potential for gust rejection of integrally-actuated membrane wings. The disturbance is a variation of the inlet angle of attack of the type

$$\alpha_\infty = \alpha_0 + \delta\alpha \left[1 - \cos\left(2\pi \mathrm{St}_\alpha t^*\right)\right], \tag{16}$$

where α_∞ is the instantaneous inlet velocity angle of incidence, $\delta\alpha$ and St_α are the amplitude and reduced frequency of the perturbation, respectively. The controller input in this case is the instantaneous value of the lift coefficient and the output is the actuation voltage. The designed variation of the inlet angle of attack is not fed-forward to the controllers, whose only input is the instantaneous lift. The range of reduced frequencies considered in this work is compatible with the disturbances experimentally investigated by Tregidgo et al. [7]. Fig. 12 shows the performance for the non-actuated and closed-loop actuated wing for selected values of $\delta\alpha$ and St_α in terms of C_l variation and controllers effort. In all cases the controllers are required to stabilise the wing performance around the reference C_l. The amplitudes and reduced frequencies of the disturbances are selected to investigate the effect of non-linearities and delays in the closed-loop wing performance.

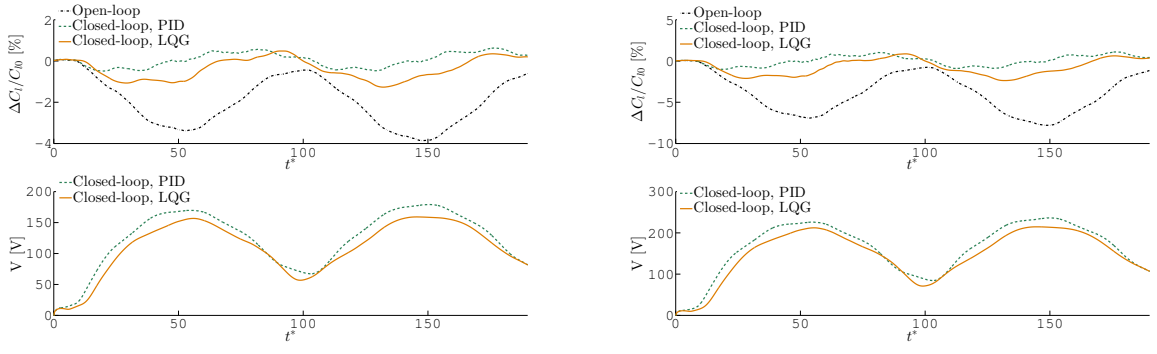

(a) $\delta\alpha = 0.1°$, $\mathrm{St}_\alpha = 0.01$.

(b) $\delta\alpha = 0.2°$, $\mathrm{St}_\alpha = 0.01$.

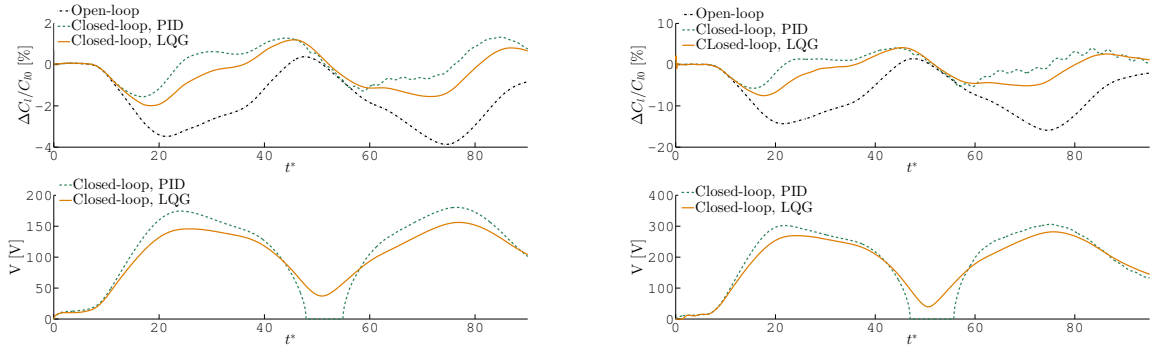

(c) $\delta\alpha = 0.1°$, $\mathrm{St}_\alpha = 0.02$.

(d) $\delta\alpha = 0.4°$, $\mathrm{St}_\alpha = 0.02$.

Figure 12: Rejection of flow disturbances. Lift evolution and controller effort for varying disturbance amplitude, $\delta\alpha$, and frequency, St_α.

The lift coefficient is constant in the initial part of the simulations due to the time required

for the inlet disturbance to convect from the boundaries to the wing. Both controller show similar reductions in the amplitude of the lift oscillations, in agreement with the closed-loop responses of the Aeroelastic ROM in sections IV.C.1 and IV.C.2. For the slowest disturbance shown (Fig. 12a and 12b), the closed-loop schemes achieve reduction of lift oscillation amplitudes of up to 70%. During the simulation, the controllers generate the voltage to relax the wing tension. This results in an increase in the camber that compensates for the reduction of lift due to the gust. In both controllers, the applied voltage shows a non-zero net value, which is linked to the average camber necessary to counteract the mean variation of the inlet angle of attack prescribed in (16). Increasing the reduced frequency of the disturbance slightly reduces the effectiveness of the controllers due to the delayed system response. They still achieve a 8% reduction of the amplitude of oscillations for $\delta\alpha = 0.1°$ and 4% for $\delta\alpha = 0.4°$ (Fig. 12d). The PID controller causes high-frequency oscillations due to the saturation of the output signal just before $t^* = 50$, while the slower performance of the LQG feedback scheme avoid the problem. PID results for $\mathrm{St}_\alpha = 0.02$ (Fig. 12c and 12d) are near the limits of stability of the controller, as it can be seen in Fig. 8. Higher frequencies do not destabilize the selected LQG feedback, but the delay in the response means that it is not able to compensate for those faster gusts either. Overall, feedback control has showed to be effective only for low-frequency disturbances due to the slow system response resulting from the interaction of the convective time-scales and the wing. This is consistent with the observations of Williams et al. [15] and Tregidgo et al. [7].

V. Conclusions

This work has presented a numerical methodology for the reduced-order modelling and control of actuated dielectric membrane wings. A system identification technique based on the Proper Orthogonal Decomposition has been used to define two low-order descriptions of the aeroelastic system. A Structure-based ROM, has been used to evaluate the impact of the amplitude of the training signal used for the identification. In a second step, the struc-

tural and the fluid descriptions have been independently reduced and coupled in monolithic system, named Aeroelastic ROM, to account for the strong fluid-structure interaction of the problem. The Aeroelastic ROM predictions have been shown to be in very good agreement with the full-model. Additionally, this ROM allows for modifications of the electrode layout and the inclusion of structural non-linearities, showing its suitability for the inclusion in a preliminary wing-design process. Importantly, the analysis of the coupled-system dynamics have showed the presence of large time delays, which had been experimentally identified in similar systems, and limits the authority of feedback controllers under high frequency excitations. Using the Aeroelastic ROM as an approximation of the full-order system dynamics, Proportional-Integral-Derivative and Linear-Quadratic-Gaussian control schemes have been designed. They have been implemented in the full model to demonstrate rejection of flow disturbance (as it will be needed in outdoor flight under gusty conditions) and tracking of a predetermined lift (to achieve manoeuvrability). The resulting closed-loop transfer functions have shown to be predictive of the behaviour of the full-order system, including the degradation of its performance at higher frequencies. This agrees with recent experimental investigations in the literature. Feed-forward schemes and an increase of the number of sensors could mitigate the limitations highlighted with the control schemes considered in this work. However, despite this limitation, intrinsically related to the physical system under investigation, the control laws have been found to be effective for low-frequencies disturbances. Overall, this preliminary investigation has demonstrated the suitability of the model reduction technique for control design and the potential of embedded actuation using DE membranes for the real time aerodynamic control of membrane wings.

Acknowledgements

The authors acknowledge the financial support of the European Office of Aerospace Research & Development of the US Air Force Office of Scientific Research, and the UK Engineering and Physical Sciences Research Council Grant EP/J002070/1, "Towards Biologically-

Inspired Active-Compliant-Wing Micro-Air-Vehicles". All results in this paper are available as open data. Information on access can be found at `http://www.imperial.ac.uk/aeroelastics/software`.

References

[1] P. Rojratsirikul, Z. Wang, and I. Gursul. Unsteady fluid structure interactions of membrane airfolis at low reynolds numbers. *Experiments in Fluids*, 46:859–872, 2009.

[2] S. Arbos-Torrent, B. Ganapathisubramani, and R. Palacios. Leadind- and trailing-edge effects on the aeromechanics of membrane aerofolis. *Journal of Fluids and Structures*, 38: 107–126, 2013.

[3] Y. Winter and O. Von Helversen. The energy cost of flight: do small bats fly more cheaply than birds? *Journal of Comparative Physiology B*, 2:105–111, 1998.

[4] R. Albertani, B. Stanford, J. Hubner, and P. Ifju. Aerodynamic coefficients and deformation measurements on flexible micro air vehicle wings. *Experimental Mechanics*, 47: 625–635, 2007.

[5] M. Hays, J. Morton, B. Dickinson, K. Uttam, and W. Oates. Aerodynamic control of micro air vehicle wings using electroactive polymers. *Journal of Intelligent Material Systems and Structures*, 24:862–878, 2013.

[6] O.M. Curet, A. Carrere, R. Waldman, and K.S. Breuer. Aerodynamic characterisation of a wing membrane with variable compliance. *AIAA Journal*, 52:1749–1756, 2014.

[7] L. Tregidgo, Z. Wang, and I. Gursul. Unsteady fluid-structure interactions of a pitching membrane wing. *Aerospace Science and Technology*, 28:79–90, 2013.

[8] H.S Park, Q. Wang ans X. Zhao, and P.A. Klein. Electromechanical instability on dielectric polymer surface: Modeling and experiment. *Computer Methods in Applied Mechanics and Engineering*, 260:40–49, 2013.

[9] R. W. Smith and W. Shyy. Computational model of flexible membrane wings in steady laminar flow. *AIAA Journal*, 33:1769–1777, 1995.

[10] Y. Lian and W. Shyy. Numerical simulations of membrane wing aerodynamics for micro air vehicle applications. *Journal of Aircraft*, 42:865–873, 2005.

[11] R. E. Gordnier. High fidelity computational simulation of a membrane wing airfoil. *Journal of Fluids and Structures*, 25:897–917, 2009.

[12] S. Buoso and R. Palacios. Electro-aeromechanical modelling of actuated membrane wings. *Journal of Fluids and Structures*, 58:188–202, 2015.

[13] M.M. Zhang, L. Cheng, and Y. Zhou. Closed-loop-controlled vortex shedding and vibration of a flexibly supported square cylinder under different schemes. *Physics of Fluids*, 16:1439–1448, 2004.

[14] S.J. Illingworth, H. Naito, and K. Fukagata. Active control of vortex shedding: an explanation of the gain window. *Physical Review E*, 90:043014–1 – 9, 2014.

[15] D. Williams, V. Quach, W. Kerstens, S.Buntain, G. Tadmor, C. Rowley, and T. Colonius. Low-reynolds number wing response to an oscillating frestream with and without feed forward control. In *47th AIAA Aerospace Sciences Meeting Including The New Horizons Forum and Aerospace Exposition*, Orlando, Florida, USA, 5-8 January 2009.

[16] D.E Raveh. Reduced order models for nonlinear unsteady aerodynamics. *AIAA Journal*, 39:1417–1429, 2001.

[17] Z. Feng and A. Soulaïmani. Investigation of nonlinear aeroelasticity using a educed order fluid model based on pod method. In *18th AIAA Computational Fluid Dynamics Conference*, Miami, Florida, USA, 25-28 June 2007.

[18] S.N. Singh, J.H. Myatt, G.A. Addington, S. Banda, and J.K. Hall. Optimal feedback control of vortex shedding using proper orthogonal decomposition models. *Journal of Fluids Engineering*, 123:612–618, 2001.

[19] S. Ahuja and C.W. Rowley. Feedback control of unstable steady states of flow past a flat plate using reduced-order estimators. *Journal of Fluid Mechanics*, 645:447–478, 2010.

[20] B. Zhang, Y. Lian, and W. Shyy. Proper orthogonal decomposition for three-dimensional membranw wings aerodynamics. In *33rd AIAA Fluid Dynamics Conference and Exhibit*, Orlando, Florida, USA, 23-26 June 2003.

[21] A. Barbagallo, D. Sipp, and P.J. Schmid. Reduced order models for closed loop control: comparison between POD, BPOD and global modes. *Progress in Flight Physics*, 3:503–512, 2012.

[22] M.N. Glauser, M.J. Young, H. Higuchi, and C.E. Tinney. POD based experimental flow control on a NACA-4412 airfoil (Invited). In *42nd AIAA Aerospace Sciences Meeting and Exhibit*, Reno, Nevada, USA, 5–8 January 2004. AIAA Paper No. 2004-0575.

[23] G. Chen, J. Sun, and Y. Li. Adaptive reduced-order-model-based control-law design for active flutter suppression. *Journal of Aircraft*, 49:973–980, 2012.

[24] H.A. Carlson, R. Roveda, and M. Glauser. Models for controlling airfoil lift and drag. In *42nd AIAA Aerospace Sciences Meeting and Exhibit*, Reno, Nevada, USA, January 2004.

[25] Dassault Systems. *SIMULIA ABAQUS FEA 6.13, User Documentation*. 2013.

[26] A.N. Gent. A new constitutive relation for rubber. *Rubber Chemistry Technology*, 69: 59–61, 1996.

[27] J. Bonet and R.D. Wood. *Nonlinear continuum mechanics for finite element analysis*. Cambridge University Press, Cambridge, UK, 2008.

[28] Z. Suo. Theory of dielectric elastomers. *Acta Mechanica Solida Sinica*, 23:549–577, 2010.

[29] CD-Adapco. *STAR-CCM+ 8.04 manual*. 2013.

[30] S.B. Pope. *Turbulent flows*. Cambridge University Press, New York, 1st edition, 2000.

[31] E.H. Dowell and D. Tang. *Dynamics of very high dimensional systems.* World Scientific Publising, Singapore, 2003.

[32] D.J. Lucia, P.S. Beran, and W.A. Silva. Reduced-order modelling: new approaches for computational physics. *Progress in Aerospace Sciences*, 40:51–114, 2004.

[33] K. Karhunen. Zur spektraltheorie stochasticher prozesse. *Annales Academiæ Scientiarum Fennicæ Series A*, 37:3–76, 1946.

[34] M.M. Loeve. *Probability theory.* Van Nostrand, Princeton, 1955.

[35] V. Buljak. *Inverse Analyses with Model Reduction.* Computational Fluid and Solid Mechanics. Springer, 2011.

[36] J.P. Thomas, E.H. Dowell, and K.C. Hall. Three-dimensional transonic aeroelasticity using proper orthogonal decomposition-based reduced-order-models. *Journal of Aircraft*, 40:544–551, 2003.

[37] K. Carlberg, C. Bou-Mosleh, and C. Farhat. Efficient non-linear model reduction via a least-squares Petrov-Galerkin projection and compressive tensor approximations. *International Journal for Numerical Methods in Engineering*, 86:155–181, 2010.

[38] D. Galbally, K. Fidkowski, K. Willcox, and O. Ghattas. Non-linear model reduction for uncertainty quantificationin large-scale inverse problems. *International Journal for Numerical Methods in Engineering*, 81:15811608, 2010.

[39] K.C Hall, J.P Thomas, and E.H. Dowell. Proper orthogonal decomposition technique for transonic unsteady aerodynamic flows. *AIAA Journal*, 38:1853–1862, 2000.

[40] P. Rojratsirikul, Z. Wang, and I. Gursul. Effect of pre-strain and excess length on unsteady fluid-structure interactions of membrane airfoils. *Journal of Fluids and Structures*, 26: 259–276, 2010.

[41] S. Skogestad and I. Postlehwaite. *Multivariable feedback control: analysis and design*. Wiley-Interscience, 2005.